



Article

Numerical Analysis of Rubberized Steel Fiber Reinforced Concrete Beams Subjected to Static and Blast Loadings

Mahmoud T. Nawar^{1,2}, Ahmed S. Eisa² , Mohamed T. Elshazli³ , Yasser E. Ibrahim¹
and Ayman El-Zohairy^{4,*}

- ¹ Engineering Management Department, College of Engineering, Prince Sultan University, Riyadh 11586, Saudi Arabia; mnawar@psu.edu.sa (M.T.N.); ymansour@psu.edu.sa (Y.E.I.)
² Structural Engineering Department, Zagazig University, Zagazig 44519, Egypt; ahmedeisa@zu.edu.eg
³ Department of Civil and Environmental Engineering, University of Missouri, Columbia, MO 65211, USA; elshazlim@missouri.edu
⁴ Department of Engineering and Technology, Texas A&M University-Commerce, Commerce, TX 75429, USA
* Correspondence: ayman.elzohairy@tamuc.edu; Tel.: +1-903-468-8683

Abstract: In recent years, the alarming number of terrorist attacks has highlighted the critical need for extensive research aimed at fortifying structures against explosion-induced loads. However, the insufficient energy absorption and brittleness of conventional concrete make it ineffective in withstanding blast loading, encouraging researchers to explore innovative strategies for augmenting the energy dissipation capabilities of construction materials. This study specifically delves into the incorporation of recycled rubber, a sustainable and environmentally friendly solution to the pressing issue of scrap tire disposal. The primary focus of this research revolves around the integration of rubber recycling and steel fibers into concrete, with the ultimate goal of enhancing the dynamic response of reinforced concrete (RC) beams. This novel approach not only contributes to the structural resilience required for resisting blast impacts, but also aligns with eco-friendly practices by reusing recycled rubber. A meticulous numerical investigation was undertaken to comprehensively assess the static and blast response of these augmented beams. The numerical study involved developing finite element (FE) models using ABAQUS version 6.14 for static implicit analysis and LS-DYNA R11 for blast explicit simulations. The ABAQUS model was validated against previous experimental testing for load–displacement and failure patterns. Similarly, the LS-DYNA model was validated for blast pressure in accordance with UFC-3-340 standards and for material response under blast loading, utilizing existing experimental data. The numerical models were designed to accommodate varying weight percentages of rubber, ranging from 5% to 20%, and a consistent 1.0% incorporation of steel fibers. This comprehensive analysis aims to provide valuable insights into the efficacy of these materials in improving the structural integrity and blast resistance of RC beams, thereby contributing to the development of more secure and sustainable construction practices. By reducing the reinforcement ratio in order to meet the minimum code requirements, it became evident that the failures of the rubberized RC beams tended to exhibit ductility on the tension side under static loading. In addition, the increase in the reinforcement ratio correlated with a higher failure load and decreased deflection. Furthermore, the findings indicated an optimal concrete mixture characterized by improved ductility, energy absorption, and blast load capacity, achieved by combining 5–10% rubber with steel fibers.



Citation: Nawar, M.T.; Eisa, A.S.; Elshazli, M.T.; Ibrahim, Y.E.; El-Zohairy, A. Numerical Analysis of Rubberized Steel Fiber Reinforced Concrete Beams Subjected to Static and Blast Loadings. *Infrastructures* **2024**, *9*, 52. <https://doi.org/10.3390/infrastructures9030052>

Academic Editor: Fabrizio Scozzese

Received: 24 January 2024

Revised: 14 February 2024

Accepted: 5 March 2024

Published: 8 March 2024



Copyright: © 2024 by the authors. Licensee MDPI, Basel, Switzerland. This article is an open access article distributed under the terms and conditions of the Creative Commons Attribution (CC BY) license (<https://creativecommons.org/licenses/by/4.0/>).

Keywords: finite element; blast loading; concrete beams; rubber; steel fibers

1. Introduction

In contemporary times, the escalating frequency of terrorist attacks and accidental explosions has highlighted the significance of evaluating the impact of blast loading on structures [1]. These catastrophic events cause serious damage to both major and minor

infrastructure, leading to injuries and fatalities within the population [2]. Numerous documented incidents of explosions involving Reinforced Concrete (RC) structures underscore the inherent vulnerability of these constructions in the face of explosive accidents [3–8]. These real-world cases underscore the urgent need for extensive research and innovative techniques to enhance the resilience and blast resistance of RC structures. The mechanical responses of RC members to dynamic loads are complex, particularly under the rapid loading conditions associated with explosion events. These conditions, characterized by the influence of inertia and short-duration forces, contribute to the complexity of the structural reactions [9]. The consequential effect is the creation of a local zone characterized by elevated pressure and temperature within the material, with the primary response coming from the point of load application. This localized response triggers the propagation of an internal shock wave throughout the concrete [10–14]. Furthermore, as the initial compressive wave reflects from the back surfaces of the concrete target, it generates a tensile wave that interacts with subsequent compressive waves. This interaction induces concrete spalling, involving the displacement of concrete pieces from the target material [9,15]. In light of these complexities, a comprehensive understanding of the dynamic responses of RC structures to blast loading is required. This knowledge forms the basis for developing effective strategies and advanced materials that can mitigate the destructive effects of explosions, ultimately fostering the creation of more resilient and safer structures in the face of contemporary security challenges.

In recent decades, there has been notable advancement in the realm of concrete materials, marked by the development of innovative formulations with enhanced mechanical properties. Researchers have dedicated their efforts to the integration of various additives, particularly fibers, into the concrete matrix to elevate both tensile strength and energy-absorbing capacities. As previously reported [16], these fibers include steel, glass, carbon, synthetic polymer fibers in a variety of shapes, and even natural fibers. A significant breakthrough in concrete construction materials was achieved through the synergistic incorporation of fibrous elements and the substitution of coarse aggregates with reactive powder materials, such as silica fume. This revolutionary composite is known as ultra-high-performance concrete (UHPC) or reactive powder concrete. Noteworthy for its distinctive composition (often featuring steel fibers, a high concentration of silica fume, and a low water–cement ratio) UHPC exhibits extraordinary mechanical qualities. Its compressive strengths can reach up to 200 MPa, tensile strengths range from 20 to 40 MPa, and fracture energies span from 20,000 to 40,000 J/m². These properties indicate a major improvement over traditional concrete materials [17]. Recent investigations into UHPC materials [18–20] have underscored their outstanding performance and revealed their substantial potential in protective engineering applications. Extensive research findings indicate that the augmentation of the flexural toughness of concrete plays a pivotal role in significantly enhancing its dynamic response [21–23]. The evolution of UHPC demonstrates the ongoing search for new materials that not only outperform traditional concrete performance, but also show promise for transformative applications in resilient and high-performance structural engineering.

Among the research efforts to produce innovative materials, Vedernikov (2022) [24] investigated the effects of regular and high pulling speeds on the morphology of pultruded glass/vinyl ester structural composites. They achieved a pulling speed of 1000 mm/min, resulting in a 1.7-times increase in output without significant compromise in mechanical performance. Another study [25] looked at how pulling speed affected the structural properties of L-shaped profiles made of pultruded glass fiber and epoxy-vinyl resin. Lower pulling speeds (200 and 400 mm/min) produced profiles with no significant differences in matrix cracking or mechanical properties, whereas higher pulling speeds (600 mm/min) resulted in delamination perpendicular to matrix cracks due to a large portion of the profile being polymerized after exiting the die.

Amid the array of innovative materials aimed at improving the flexural toughness and overall performance of concrete, the integration of rubber has emerged as a partic-

ularly noteworthy focus [26–28]. Extensive research has delved into the utilization of crumb rubber, derived from discarded tires, as a constituent in concrete mixtures. Ishiaq Alam [29] underscored that incorporating crumb rubber as fine aggregates led to a notable enhancement in toughness. Meanwhile, research by Trilok Gupta [30] unveiled a substantial improvement in concrete impact resistance and ductility. This was evident through heightened performance metrics, including an increased number of blows sustained before failure and a delayed onset of the first crack. These findings illuminate the potential for incorporating rubberized concrete in protective applications, showcasing its promise in enhancing the resilience and durability of concrete structures.

Despite the promising advantages offered by utilizing rubberized concrete, previous studies have reported some drawbacks and limitations [31–36]. In a study by Eshmaiel Ganjian [37], coarse aggregates were partially replaced with chipped tires of comparable grading size to the original aggregate, at varying weight percentages (5%, 7.5%, and 10%). The findings indicated a decrease in compressive strength and tensile strength with an increase in rubber content. Similar concerns were observed in other studies, where the addition of rubber led to reduced compressive strength. This decline is attributed to the soft elasticity of rubber particulates, making it challenging for concrete to meet structural requirements. Consequently, these drawbacks limited the application of rubber in concrete for structural components that do not require high compressive strength.

In our pursuit of harnessing the benefits of incorporating rubber into concrete while maintaining high compressive and tensile strength, our recent experimental investigation [28] meticulously explored the combined effect of crumb rubber and steel fibers on the performance of reinforced concrete beams. The crumb rubber, with sizes ranging from 2 to 3 mm, was introduced as a partial replacement for fine aggregates, with varying weight percentages—specifically, 5%, 10%, 15%, and 20%. Concurrently, hooked-end steel fibers are integrated at a consistent volume fraction of 1%. The outcomes of our tests revealed that incorporating crumb rubber as a partial replacement for fine aggregates at 5% and 10% demonstrated satisfactory performance in reinforced concrete beams. Moreover, an intriguing observation emerged: the introduction of steel fibers into rubberized concrete, particularly with rubber percentages exceeding 10%, enhanced both the overall performance and toughness of the structural elements. These findings highlight the complex relationship between crumb rubber, steel fibers, and concrete composition. They not only validate the feasibility of achieving optimal results with modest rubber content, but also highlight the combined benefits of reinforcing rubberized concrete with steel fibers, particularly in scenarios where higher rubber percentages are involved. This understanding contributes to ongoing efforts to find a balance between innovation and structural integrity in the field of concrete technology.

Beyond the notable performance enhancements, the integration of rubber into concrete offers substantial environmental advantages. As documented in previous studies [38–42], the conventional disposal of used tires in landfills has been linked to a range of severe economic and environmental challenges. These issues extend beyond potential environmental hazards, encompassing heightened risks of accidental fires that contribute to increased pollution emissions, particularly due to the flammability of tires [43]. The disposal of tires has evolved into a significant environmental concern over time. In light of these challenges, incorporating rubber into concrete emerges as a holistic solution with multifaceted benefits. This innovative approach not only delivers performance advantages, but also plays a crucial role in mitigating the severe environmental issues associated with tire disposal. By repurposing rubber in concrete applications, we not only enhance the material's functionality, but also contribute to a more sustainable and environmentally responsible solution to the longstanding challenges posed by tire disposal.

The environmental benefits of using recycled rubber in concrete are numerous and critical for sustainability. However, it is critical to assess the environmental implications and practicality of the broad use of these materials in the construction industry. One significant environmental trade-off to consider is the energy consumption and emissions

associated with the recycling process [44–47]. While using recycled rubber decreases the need for raw materials and diverts waste from landfills, the recycling process is often energy-intensive and creates greenhouse emissions [46]. As a result, a comprehensive life cycle assessment (LCA) is required to determine the overall environmental impact, including energy consumption, emissions, and potential environmental benefits [48]. Another factor to consider is the rubberized concrete's durability and long-term performance when compared to ordinary concrete. While rubberized concrete may have some advantages, such as increased flexibility and fracture resistance, its long-term durability and structural integrity under different environmental circumstances must be carefully considered [49,50].

Numerical simulations stand as an effective tool for conducting comprehensive investigations into material responses under extreme loadings. For instance, Thiagarajan et al. [51] undertook an initial exploration, employing numerical simulations to investigate high-strength steel, high-strength concrete, and normal-strength concrete slabs, subsequently comparing their findings with experimental data. Schleyer et al. [52] conducted numerical calculations involving explosive testing on ultra-high-performance fiber-reinforced concrete panels, aiming to determine a safe explosion distance that ensures lasting damage without complete structural collapse. In a study by Wang et al. [53], a numerical investigation delved into the impact of fiber aspect ratio on the mechanical properties of steel-reinforced fiber concrete (SRFC) under dynamic loads. Their findings were compared to experimental data. Teng et al. [54] advanced the field by developing a numerical model for high-velocity impact scenarios, specifically focusing on steel fiber-reinforced concrete using LS-DYNA R11. Meanwhile, Mao et al. [55] delved into numerical simulations of high-performance fiber-reinforced concrete panels subjected to blast loads. Remarkably, all these research endeavors unveiled a considerable agreement between numerical models and experimental works. The success of the numerical technique lies in its ability to comprehensively replicate experimental results with a high degree of precision, achieved through the use of appropriate constitutive material models capable of accurately capturing the impact of strain rate.

In this study, a thorough numerical investigation was conducted to assess both the static and blast responses of reinforced concrete (RC) beams reinforced with rubberized concrete and steel fibers. The incorporation of rubber into the concrete mixture involved replacing fine aggregates at varying weight percentages, ranging from 5% to 20%. Additionally, a consistent volume fraction of 1% steel fibers was introduced into the composition. The numerical study involved developing finite element (FE) models using ABAQUS version 6.14 for static implicit analysis and LS-DYNA R11 for blast explicit simulations. The ABAQUS model was validated against previous experimental testing [28] for load displacement and failure patterns. Similarly, the LS-DYNA model was validated for blast pressure in accordance with UFC-3-340 standards and for material response under blast loading, utilizing existing experimental data [56]. This rigorous validation process ensured the reliability and accuracy of the numerical models. The study employed diverse methods for modeling the blast response of RC beams. The static and dynamic responses of these beams were subjected to comprehensive discussion, shedding light on the complex interaction of materials and structural dynamics in the face of blast loading scenarios. The combined expertise of both software tools and the detailed blast modeling approaches provided a robust foundation for understanding and evaluating the multi-faceted performance of rubberized and steel fiber-reinforced RC beams under static and dynamic conditions.

2. Finite Element Analysis

This paper presents a comprehensive numerical exploration of the static and blast response of reinforced concrete beams. The investigation unfolds in two stages, involving computer simulations meticulously validated against existing experimental data. In the initial stage, a finite element model, implemented using ABAQUS version 6.14, was developed and rigorously validated against prior experimental studies [28]. This phase aims to study the impact of incorporating crumb rubber and steel fibers on the structural

behavior of reinforced concrete beams, ensuring the applicability for structural engineering design practice and safety margins. Subsequently, the second stage introduces an LS-DYNA model, validated through comparison with Yan Liu’s work [56]. This model investigates the response of reinforced concrete beams made of rubberized concrete and steel fibers when subjected to blast loading. Through this dual-stage approach, our investigation aims to provide comprehensive insights into the performance of rubberized and rubberized steel fiber-reinforced concrete beams under both static and dynamic conditions, particularly shedding light on their behavior in the face of explosive loading scenarios.

2.1. Static Numerical Simulation

A nonlinear three-dimensional finite element (FE) model was meticulously developed using the ABAQUS CAE 6.14 software to simulate RC beams incorporating crumb rubber and steel fibers. This study included ten different concrete mixtures, comprising a control mix denoted as PC, four variations of rubberized concrete mixes (designated as RCX, with X representing the percentage of rubber as a partial replacement of fine aggregates, ranging from 5% to 20%), a concrete mix reinforced with steel fibers (SFC) featuring a 1% steel fiber volume fraction, and four mixtures of rubberized steel fiber RC mixes (SFRCX). Table 1 outlines the mechanical properties of the concrete mixtures used in the study.

Table 1. The mechanical properties of the used concrete mixtures.

No.	Mix	Compressive Strength (MPa)	Modulus of Elasticity (MPa)	Splitting Tensile Strength (MPa)	Modulus of Rupture (MPa)
1	PC	44.20	17,612	3.40	6.89
2	RC5	39.80	15,258	2.55	6.72
3	RC10	33.70	13,348	2.26	6.33
4	RC15	25.70	10,072	2.12	5.78
5	RC20	18.00	6970	1.98	5.44
6	SFC	47.20	22,845	6.65	8.67
7	SFRC5	44.30	20,704	4.81	8.05
8	SFRC10	39.50	18,200	4.22	7.11
9	SFRC15	32.20	15,043	3.92	6.57
10	SFRC20	24.17	11,505	3.47	6.22

In the experimental work in [28], a standard reinforced concrete beam underwent a four-point loading flexural test. The beam possessed a rectangular cross-section with a width of 100 mm, an effective depth of 200 mm, and a length of 1600 mm, providing a clear span of 1500 mm. The RC beams were designed to fail due to flexure rather than shear, by ensuring shear capacity greater than flexural capacity. For reinforcement, 10 mm in-diameter deformed steel rebars made of high-grade steel ($f_y = 400$ MPa) were utilized as the primary reinforcement. Hangers, consisting of 8 mm in-diameter non-deformed steel rebars made of mild steel ($f_y = 280$ MPa), were spaced longitudinally at 100 mm intervals. A minimum concrete clear cover of 15 mm was maintained throughout the beam structure. Testing was carried out in accordance with ASTM C78 standards. The results showed an increase in deflection, cracking behavior, and ductility of RC beams as rubber content increased up to 10%. However, exceeding this threshold led to a shift towards a brittle failure mode on the compression side. This drawback motivated this research to numerically investigate the influence of reinforcement ratio on the failure mode.

In the FE model, the concrete elements were represented using eight-node solid elements (C3D8). A convergence study was conducted using four different mesh sizes: 30 mm, 20 mm, 15 mm, and 10 mm (Figure 1). The results indicated the optimal mesh size

to be 20 mm. Additionally, two-dimensional truss elements (T3D2) with the same mesh size (20 mm) were employed to simulate the reinforcing by steel bars and stirrups. To model the interaction between the reinforcement and concrete, an embedded constraint was applied, ensuring the complete coupling of the steel reinforcements into the host concrete elements (Figure 2). To establish precise boundary conditions, two steel plate supports were incorporated. Each plate had dimensions of 20 mm in thickness, 50 mm in width, and 100 mm in length. The ABAQUS model’s boundary conditions were defined using nodal displacement loads. In this study, hinged support was assigned by imposing constraints on the displacement degrees of freedom (DOFs) in the X, Y, and Z directions. Additionally, roller support was implemented by imposing constraints on the displacement DOFs in the X and Y directions. Figure 3 provides a visual representation of the various components within the FE model.

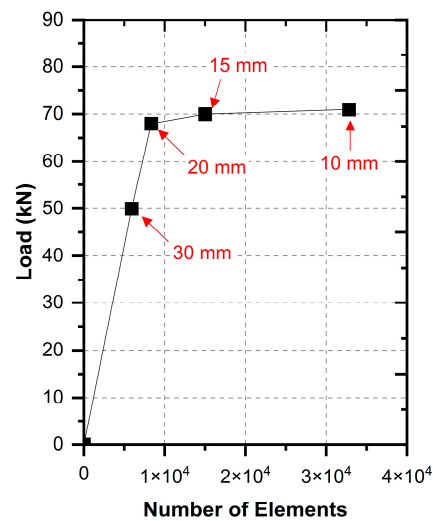


Figure 1. Mesh sensitivity analysis.

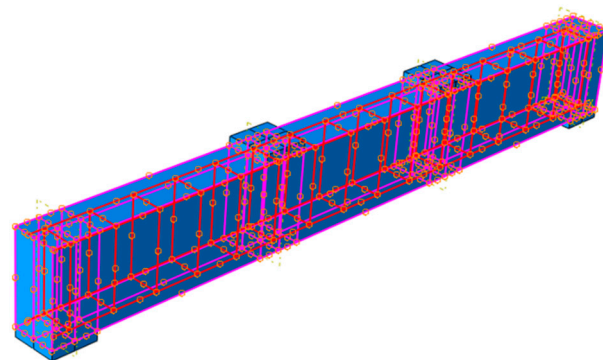


Figure 2. Reinforcement–concrete interface using embedded constraint.

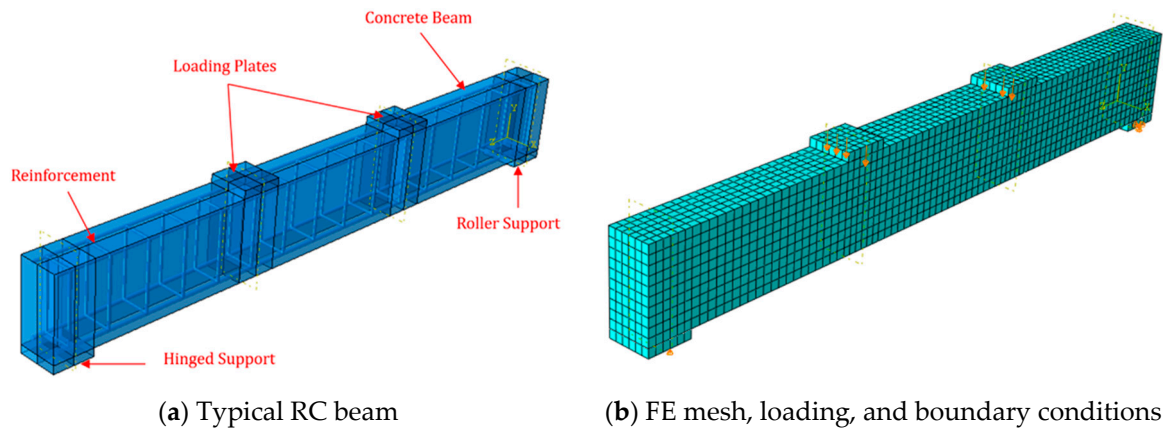


Figure 3. FE model using ABAQUS for static analysis.

The concrete damage plasticity (CDP) model was employed herein to present the inelastic behavior of concrete. In the CPD model, the main failure mechanism of concrete is assumed to be caused by cracking in tension and crushing in compression. The yield or failure is controlled by two variables: the equivalent tensile plastic strain and the equivalent compressive plastic strain. Ten CDP models, representing the ten concrete mixtures included in this study, were calibrated using the compression and splitting tensile tests performed experimentally and reported in [28]. The simulated response of concrete to uniaxial compression loading by the CDP model is shown in Figure 4. The plastic behavior of concrete was modeled based on the Drucker–Prager hyperbolic function (Equation (1)).

$$G = \sqrt{(e f_{ctm} \tan(\psi))^2 + q^2} - p \tan(\psi) \quad (1)$$

where G is the plastic flow potential, the flow potential eccentricity (e) was assumed as 0.1, ψ is the dilation angle, q is the von Mises effective stress, and p is the hydrostatic pressure. In addition to the flow potential parameters, the default values of the ratio between the biaxial and uniaxial compressive strength ($f_{bo}/f_{co} = 1.16$) and the ratio of the second stress invariant on the tensile meridian to that on the compressive meridian ($K_c = 2/3$) were used. Typically, the dilation angle (ψ) serves as a critical parameter influencing both the strength and ductility of the simulated concrete material. Different values of dilation angles ranging from 25 to 31 were used to represent the change in the plastic volumetric strain. The dilation angle of rubberized concrete mixtures was found to be higher than that of steel fiber concrete. A lower dilation angle corresponded to higher-strength concrete, as it signifies less lateral expansion of the material under load, resulting in a denser and stronger concrete matrix. Conversely, higher dilation angles are associated with increased ductility, allowing for more lateral expansion and deformation before failure. This enhanced ductility enables the material to absorb more energy and exhibit a more ductile response under load. Therefore, precise adjustment of the dilation angle is crucial to ensure the accuracy of material model predictions.

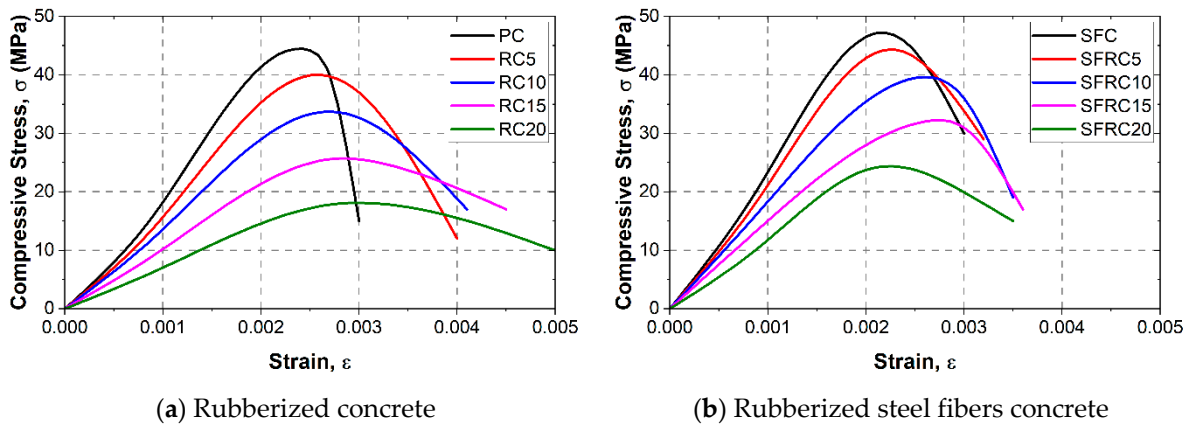


Figure 4. Compression stress–strain curves of concrete.

Reinforcement elements were assumed to be elastic perfectly plastic material with identical behavior in tension and compression, as shown in Figure 5.

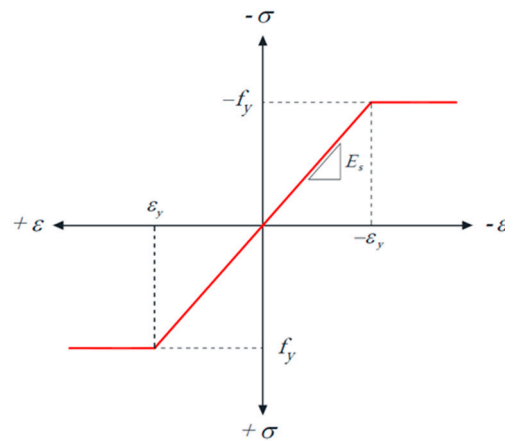


Figure 5. Stress–strain relationship for steel reinforcement.

2.2. Blast Numerical Simulation

The dynamic responses of the tested RC beams in [28] were investigated using LS-DYNA to explore the effect of crumb rubber and steel fibers. The experimental work conducted by Yan Liu [56] was used to validate the developed FE models. In the experimental work, one-half-scale beams were tested at different levels of blast loading, and the damage levels and modes were observed. The beams had a length of 1700 mm, a width of 150 mm, and a thickness of 150 mm. The tested beams were doubly reinforced with two 8 mm in-diameter non-deformed reinforcement with exterior 6 mm diameter hooks spaced at a distance of 180 mm from one another in the major bending plane. The clear cover to reinforcement was maintained at 20 mm. The compressive strength of the concrete material used in the experiment was 30 MPa, and the density was 24.5 kN/m³. All beams were tested under transverse shock-wave loads using TNT. A concrete base, providing a simply supported boundary condition, supported the beams. The recorded reflected pressure and deflection time histories were used to validate the FE model.

The FE model was built with the same dimensions and properties that were used in experimental work [56], as shown in Figure 6. The concrete beam was modeled using hexahedral solid elements with one integration point, with a maximum mesh size of 7.5 mm. A stiffness-based hourglass (HG) control was used to manage the non-physical hourglass deformations caused by the use of under-integrated elements. This approach not only reduces the computational cost, but also contributes to a decrease in the overall model’s energy, resulting in a more flexible FE model. Beam elements with truss formulation were used to

represent the reinforcement. The *CONSTRAINED_LAGRANGE_IN_SOLID algorithm was selected for this study to couple between reinforcement and concrete. The concrete was modeled using material type 084 *MAT_WINFIRTH_CONCRETE. The nonlinear response of the ten concrete mixtures was included by defining stress–strain curves using the experimental results. This model includes a plasticity portion based on Ottosen’s failure surface [57], which is a four-parameter model with a curved meridian and noncircular deviatoric section, which enables the representation of the different plasticity behaviors of the different concrete mixtures. Reinforcements were modeled using the elastic–plastic material model with kinematic hardening (*MAT_PLASTIC_KINEMATIC). This model also allows for consideration of the strain-rate effect using the Cowper–Symonds formula [58].

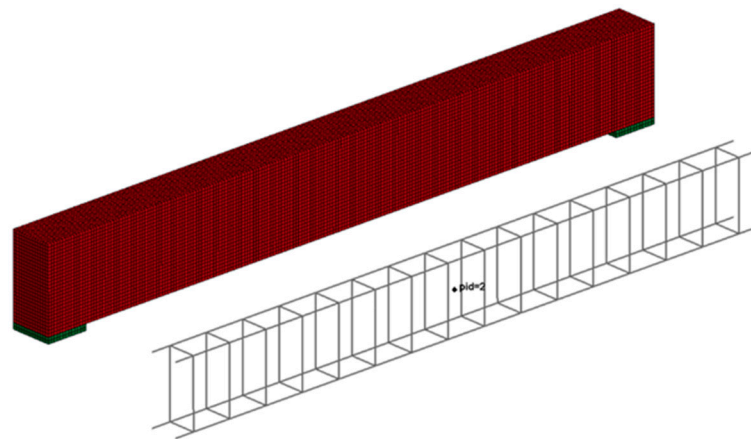


Figure 6. The typical RC beam FE model using LS-DYNA.

Three modeling approaches can be used to simulate blast loading: Load Blast Enhanced (LBE), Arbitrary Lagrangian–Eulerian (ALE), and coupling of the LBE and ALE methods. The LBE method is the simplest approach, which requires less computational time. In this method, the structure was only modeled and the mass and coordinates of the explosion were defined. After that, LS-DYNA calculated the pressure from the explosion and applied it to the selected surface; see Figure 7a.

The ALE method is a complex method that requires the modeling of the structure, the explosive material, and the containing air domain, as shown in Figure 7b. In this study, for the ALE models, the air was modeled using solid elements with ALE formulation and material type 009 *MAT_NULL, which requires an equation of state. The linear polynomial equation of state was used to correlate between pressure and density of air as defined in Equation (2). Table 2 shows the polynomial EOS parameters used in this study.

$$P = C_0 + C_1\mu + C_2\mu^2 + C_3\mu^2 + [C_4 + C_5\mu + C_6\mu^2]E \quad (2)$$

where P is the pressure; E is the internal energy per initial volume; $C_0, C_1, C_2, C_3, C_4, C_5,$ and C_6 are constants; $\mu = \rho/\rho_0 - 1$, where ρ and ρ_0 are the current and the initial densities, respectively. In this study, air parameters, $C_0, C_1, C_2, C_3,$ and $C_6 = 0$, and $C_4 = C_5 = \gamma - 1$, where γ is the ratio of specific heat at constant pressure per specific heat at constant volume, $\gamma = 1.4$.

Table 2. The linear polynomial EOS parameters.

Parameter		Value
C ₀	Mass Density	1.29 Kg/m ³
C ₁	Null Constant	0
C ₂	Null Constant	0
C ₃	Null Constant	0
C ₄	Null Constant	0.4
C ₅	Null Constant	0.4
C ₆	Null Constant	0
E ₀	Initial internal energy.	2.50 × 10 ⁵ Pa
V ₀	Initial relative volume.	1

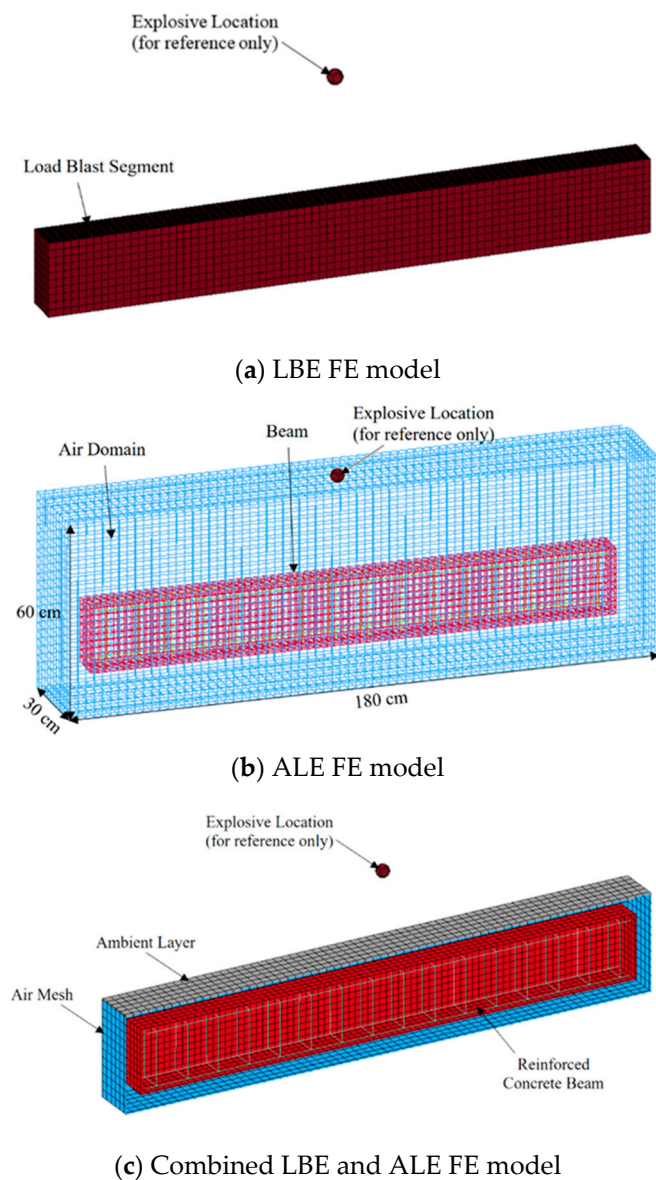


Figure 7. Different modeling approaches to simulate BLAST loading.

The high explosive was used to model TNT using solid elements with ALE formulation, with material model type 008 *MAT_HIGH_EXPLOSIVE_BURN. This material model

controls the release of the chemical energy for simulating detonations. The JWL equation of state (Equation (3)) was used to represent the change in the density of the HE over time.

$$P = A \left(1 - \frac{\omega}{R_1 V} \right) e^{-R_1 V} + B \left(1 - \frac{\omega}{R_2 \omega} \right) e^{-R_2 V} + \frac{\omega}{V} E \tag{3}$$

where A, B, R₁, R₂, and ω are empirically defined constants that are different for each explosive type; V is the relative volume; and E is the detonation energy per initial volume. Table 3 lists the JWL EOS parameters used in this study. The initial distribution of air and TNT was defined by the *INITIAL_VOLUME_FRACTION_GEOMETRY keyword, through the definition of the initial shape and location of the TNT explosive charge. The detonation was initialized using the *INITIAL_DETONATION keyword, with the detonation point set at the center of the explosive charge. Due to the heavy computational costs of the ALE method, it was not possible to extend the boundaries of the surrounding air domain too far beyond the outer lines of the Lagrangian part. However, this can result in spurious reflections of the pressure waves at the boundaries of the air domain. Therefore, the *BOUNDARY_NON_REFLECTING keyword was applied to all surfaces of the air domain.

Table 3. The JWL EOS parameters.

Parameter		Value
A	EOS Coefficient	3.712×10^{11}
B	EOS Coefficient	3.231×10^9
R ₁	EOS Coefficient	4.15
R ₂	EOS Coefficient	0.95
OMEG	Null Constant	0.30
E ₀	Null Constant	7.0×10^9 Pa
V ₀	Null Constant	1
E ₀	Initial internal energy.	2.50×10^5 Pa
V ₀	Initial relative volume.	1

Finally, the interaction between the air and the Lagrangian part was obtained using the *CONSTRAINED_LAGRANGE_IN_SOLID keyword. Coupling the LBE and ALE gives the benefits of both methods; it is simpler than ALE and gives more accurate results compared to LBE. In this method, the structure and a small portion of the air domain around the structure were just modeled, and the blast was applied as the LBE method, as shown in Figure 7c. As performed in the ALE model, the boundary conditions of the exterior air surface were treated as non-reflecting boundaries. All parameters and definitions of air and EOS were equal to those used in the ALE model in both the air domain and ambient layer. Nonetheless, the ambient layer was activated by setting AET = 5 in the *SECTION_SOLID. Later, the exterior segments of the ambient layer were identified in the *LOAD_BLAST_SEGMENT.

3. Static FE Results

3.1. Validation

Both the experimental and numerical results are summarized in Table 4. The developed static FE model was validated against the experimental results [28]. Figure 8 compares the FE and experimental load–displacement curves. These comparisons highlight the agreement between the FE model and the experimental data. The results show a notable level of agreement, with a maximum error of less than 15%. This could be attributed to the random distributions of steel fibers. The experimental results in [28] previously identified two separate forms of flexural failure depending on the rubber content, tension side and compression side failures. It can be seen that the developed FE models successfully predicted these two failure modes over a range of concrete mixtures, as shown in Figure 9. Moreover, the relationships between the load and the measured strains are compared

in Figures 10 and 11 for the top fiber of concrete and longitudinal reinforcement rebars, respectively.

Table 4. Comparisons between the FE and experimental results.

No.	Model Label	Failure Load (kN)			Maximum Deflection (mm)		
		EXP.	FE	Difference %	EXP.	FE	Difference %
1	PC	64	68	6.25	15.7	14.8	6
2	RC5%	60	62	3.33	15.9	14.9	6.7
3	RC10%	56	59	5.36	18.9	17.2	9.88
4	RC15%	53	57	7.55	20	18.8	6.38
5	RC20%	51	54	5.88	22.8	21.8	4.58
6	SFC	81	88	8.64	12.9	11.8	9.32
7	SFRC5%	72	76	5.55	13.8	12.9	6.97
8	SFRC10%	67	72	7.46	17	15.5	9.67
9	SFRC15%	62	69	11.29	19	17.76	6.98
10	SFRC20%	58	64	10.34	21.9	21.11	3.74

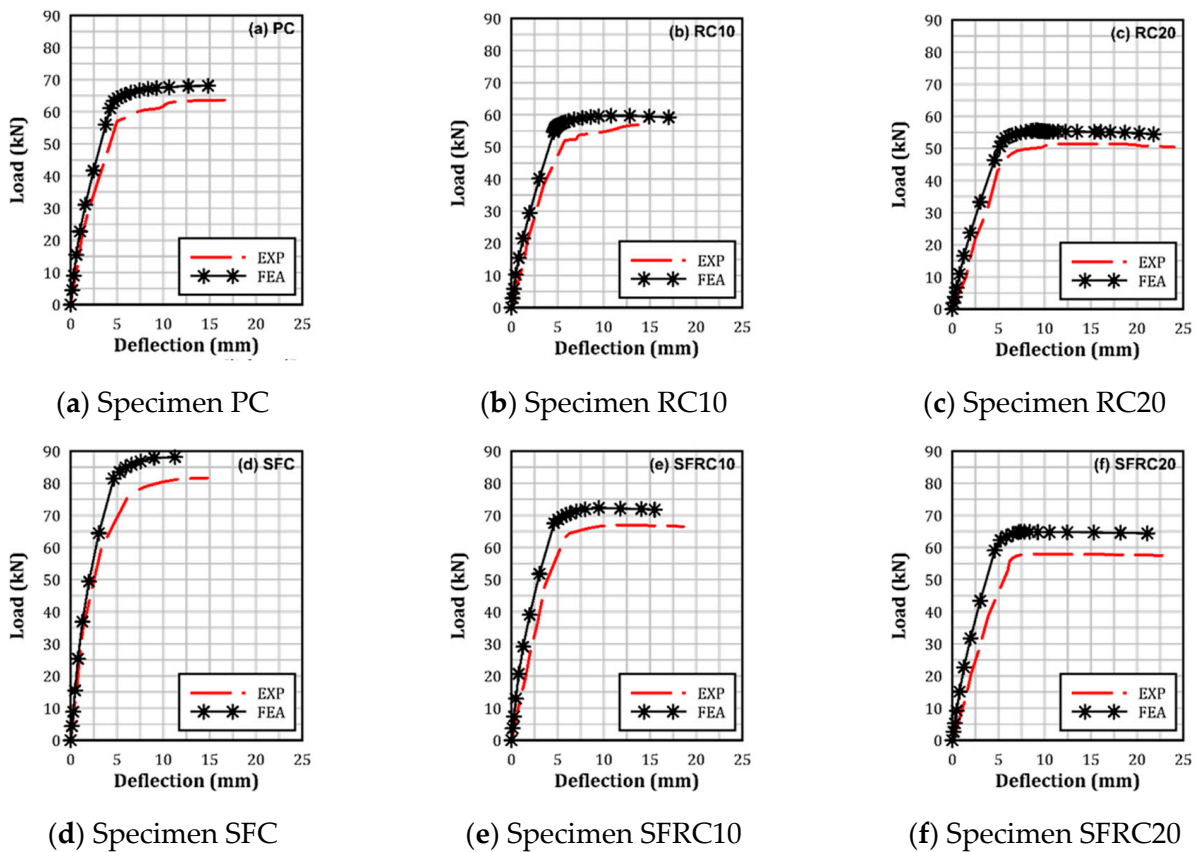


Figure 8. Comparisons between the FE and experimental results under static loadings.

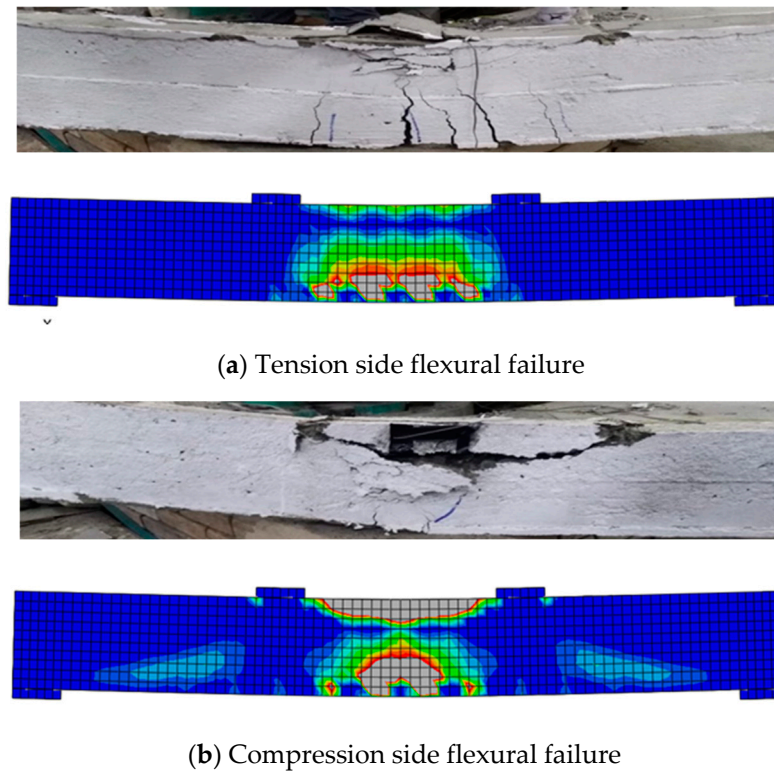


Figure 9. Comparisons between the FE and experimental modes of failure.

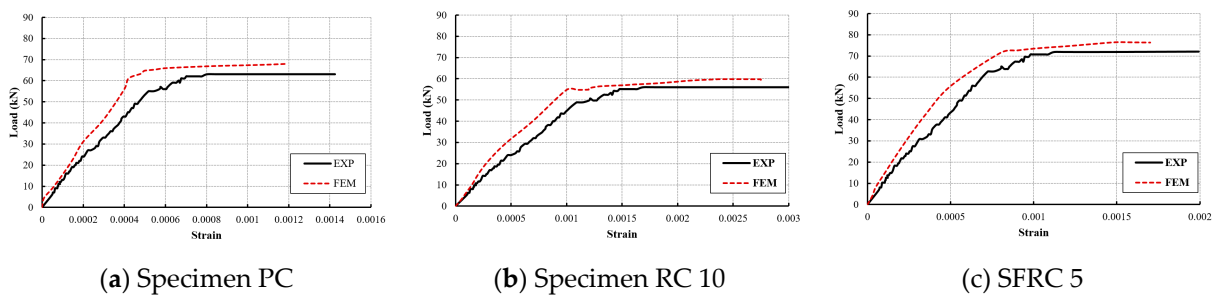


Figure 10. Validation of the load–strain relationships for the compression extreme fiber of concrete.

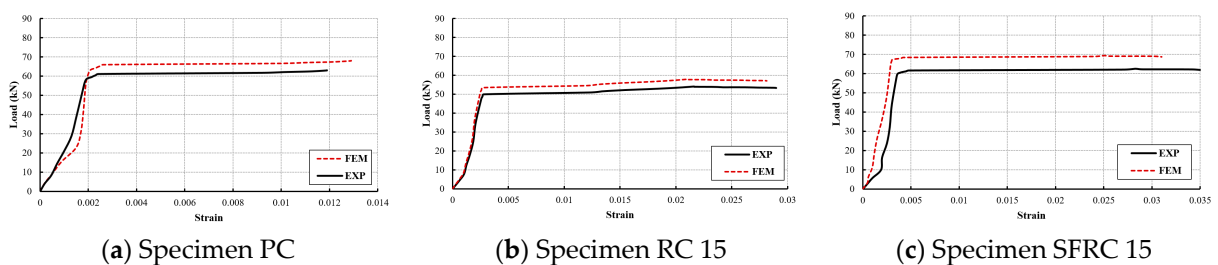


Figure 11. Validation of the load–strain relationships for the steel rebars.

3.2. Effect of Reinforcement Ratio

The decrease in compressive strength with increasing rubber content limits the use of rubberized concrete with high rubber replacements. In our earlier investigation [26], we identified that 10% rubber content is best for maintaining the balance between environmental benefits and structural performance. In addition, the escalation in the rubber percentage led to a shift from ductile failure to brittle failure on the compression side [28]. Therefore, the study recommended the use of steel fibers to maintain structural integrity.

Consequently, in this study, we investigated the impact of varying reinforcing ratios ($\mu\%$) across distinct concrete mixtures as a possible way to improve the performance of high rubber-content concrete beams. Three specific reinforcement ratios were selected for examination: 0.5% (utilizing two 8 mm diameter rebars), 0.78% (employing two 10 mm diameter rebars), and 1.13% (utilizing two 12 mm diameter rebars), as outlined in Table 5.

Table 5. The results of different reinforcement ratios.

No.	Model	μ (%)	Failure Load	Maximum Deflection	ϵ_{cmax}	ϵ_{tmax}	Failure Mode
1	PC	0.5	43.5	15.2	0.0013	0.0135	Tension Side
		0.78	68.0	14.81	0.0012	0.0129	Tension Side
		1.13	88.0	9.00	0.0010	0.0100	Tension Side
2	RC5	0.5	37.4	15.50	0.0020	0.0206	Tension Side
		0.78	62.0	14.89	0.0019	0.0191	Tension Side
		1.13	79.0	9.60	0.0016	0.0152	Tension Side
3	RC10	0.5	35.2	18.28	0.0031	0.0290	Tension Side
		0.78	59.0	17.04	0.0028	0.0261	Tension Side
		1.13	71.0	11.80	0.0024	0.0220	Tension Side
4	RC15	0.5	34.0	21.00	0.0069	0.0320	Tension Side
		0.78	57.8	18.87	0.0059	0.0281	Compression
		1.13	68.0	14.20	0.0053	0.0245	Compression
5	RC20	0.5	32.7	27.37	0.0210	0.0400	Tension Side
		0.78	55.6	21.81	0.0172	0.0322	Compression
		1.13	62.0	19.00	0.0160	0.0300	Compression
6	SFC	0.5	65.2	11.35	0.0010	0.0138	Tension Side
		0.78	88.2	11.27	0.0009	0.0130	Tension Side
		1.13	106.0	8.00	0.0008	0.0105	Tension Side
7	SFRC5	0.5	53.0	13.30	0.0018	0.0260	Tension Side
		0.78	76.6	12.98	0.0017	0.0240	Tension Side
		1.13	90.0	9.50	0.0015	0.0200	Tension Side
8	SFRC10	0.5	48.7	16.20	0.0024	0.0330	Tension Side
		0.78	72.3	15.50	0.0022	0.0290	Tension Side
		1.13	83.0	12.00	0.0019	0.0255	Tension Side
9	SFRC15	0.5	46.1	19.80	0.0056	0.0370	Tension Side
		0.78	69.3	18.76	0.0050	0.0310	Tension Side
		1.13	77.0	15.50	0.0044	0.0285	Tension Side
10	SFRC20	0.5	42.7	24.61	0.0160	0.0430	Tension Side
		0.78	64.9	21.11	0.0137	0.0340	Balanced
		1.13	69.0	18.80	0.0123	0.0325	Compression

By reducing the reinforcement ratio in order to meet the minimum code requirements, it becomes evident that failures tend to exhibit ductility on the tension side. Furthermore, the findings illustrate that an increase in the reinforcement ratio correlates with a higher failure load and decreased deflection, as depicted in Figure 12. Specifically, when the reinforcement ratio was decreased from 0.78% to 0.5%, the results indicated a deflection increase ranging from 3% to 26% for rubberized concrete beams and 1% to 17% for rubberized steel fiber concrete beams, with varying crumb rubber percentages from 0% to 20%, as illustrated in Figure 13a. Additionally, the maximum compressive strain varied from 6% to 22% for rubberized concrete beams and 5% to 17% for rubberized steel fiber concrete beams, as shown in Figure 13b. Regarding the strains in steel rebars, the maximum tensile strain ranged from 5% to 24% for rubberized concrete beams and 6% to 26% for rubberized steel fiber concrete beams, as depicted in Figure 13c.

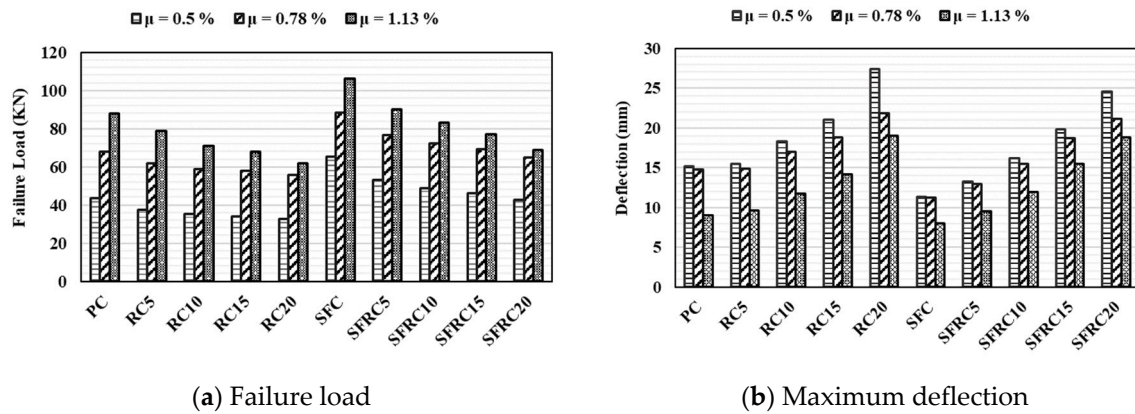


Figure 12. Effect of the different reinforcement ratios.

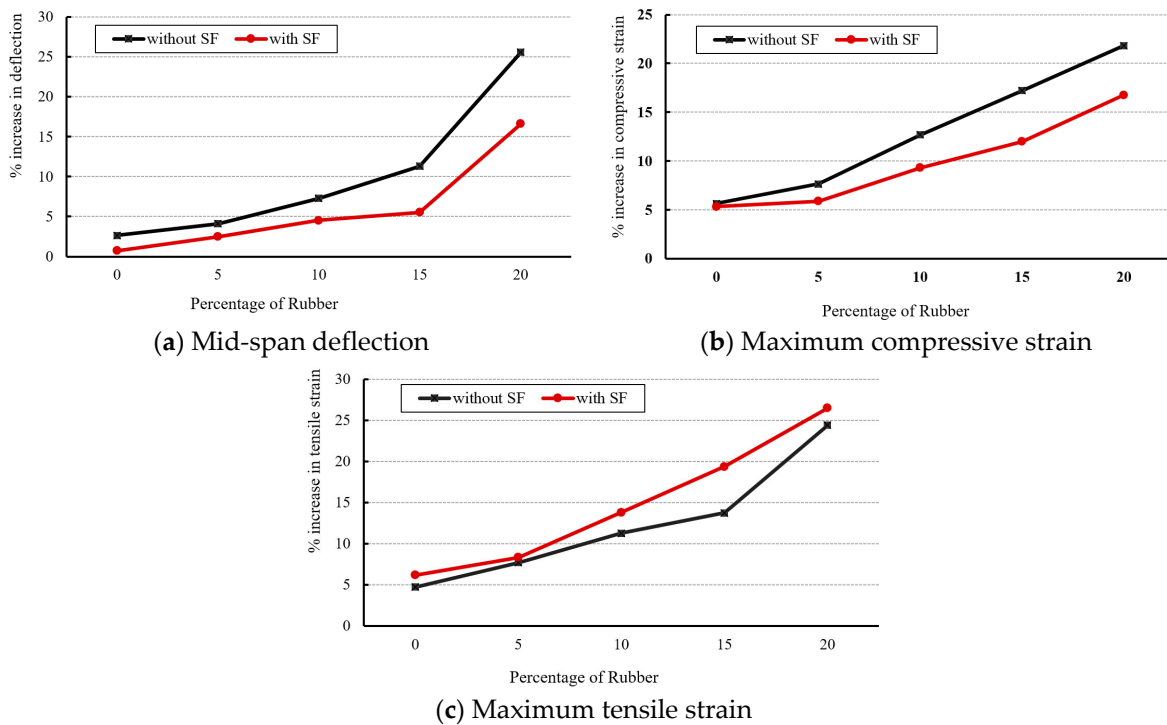


Figure 13. The effect of reinforcement ratio varied from 0.78% to 0.5% for specimens with and without steel fibers.

Conversely, with an increase in the reinforcement ratio from 0.78% to 1.13%, the outcomes indicate a decrease in deflection ranging from 39% to 13% for rubberized concrete beams and from 29% to 11% for rubberized steel fiber concrete beams, covering crumb rubber percentages from 0% to 20%, as depicted in Figure 14a. Furthermore, the findings reveal a decline in maximum compressive strain, ranging from 15% to 7% for rubberized concrete beams and from 17% to 10% for rubberized steel fiber concrete beams, when crumb rubber percentages varied from 0% to 20%, as illustrated in Figure 14b. However, the reduction in maximum tensile strain ranged from 22% to 7% for rubberized concrete beams and from 19% to 4% for rubberized steel fiber concrete beams, as shown in Figure 14c.

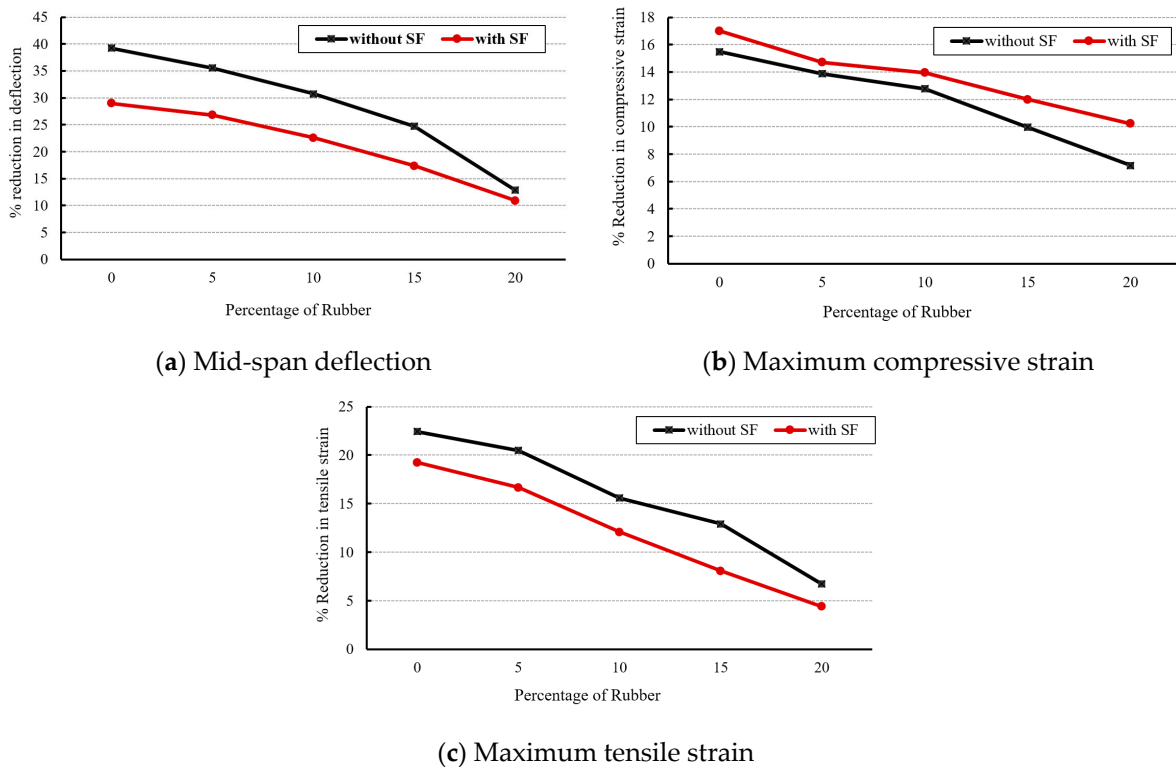


Figure 14. The effect of the reinforcement ratio varied from 0.78% to 1.13% for specimens with and without steel fibers.

The considerable reduction in maximum deflection found in rubberized concrete beams, as the reinforcing ratio increased has important implications for structural engineering design practice and safety margins. The reduction in maximum deflection implies an increase in the stiffness and overall structural performance of rubberized concrete beams with higher reinforcement ratios. This shows that raising the reinforcement ratio can significantly improve the structural integrity and load-bearing capability of the beams, resulting in lower deflection under applied loads. From a design standpoint, this study emphasizes the significance of carefully selecting and optimizing the reinforcement ratio to satisfy required structural performance and safety requirements.

Furthermore, the observed decrease in maximum deflection indicates an improvement in the beams’ resistance to deformation and potential failure under load. This is especially important in real-world applications where structures are subjected to a variety of loading situations, including static and dynamic loads, environmental factors, and possible risks like earthquakes or blast events. Higher reinforcement ratios can help improve the overall stability and safety of structures by reducing deflection, and lowering the risk of structural failure while increasing structural resilience and benefiting from the increased toughness of rubberized concrete.

4. Dynamic FE Results

4.1. FE Model Validation

The validation of the LS-DYNA model was performed in two stages. Firstly, the blast pressure was validated by comparing it to the UFC-3-340-02 calculations. During this step, a solid element mesh with a Eulerian formulation was used to model the air zone. This was accomplished by constructing a 1000 mm × 1000 mm × 1000 mm air cube at atmospheric pressure, with an explosive placed in one corner, as shown in Figure 15. Three different explosive sizes were used for this simulation: 8 kg, 20 kg, and 40 kg. Air overpressures were computed at various distances and explosive sizes. Three points were selected at different distances (200 mm, 400 mm, and 600 mm) from the center of the explosive. Figure 16

shows the pressure distribution over time at the selected points and the dissipation of the energy. The front pressure gradually decreased over time. When the LS-DYNA results are compared to those from UFC 3-340-02, as shown in Figure 17, the results show an acceptable similarity with a difference of less than 13%, indicating that LS-DYNA produces reliable predictions of free air pressure. In the second stage, the responses of the reinforced concrete beam under blast loading, in terms of pressure–time history and maximum mid-span deflection, were compared to Yan Liu’s experimental work [56]. As can be seen from Figure 18, the results indicated a good agreement.

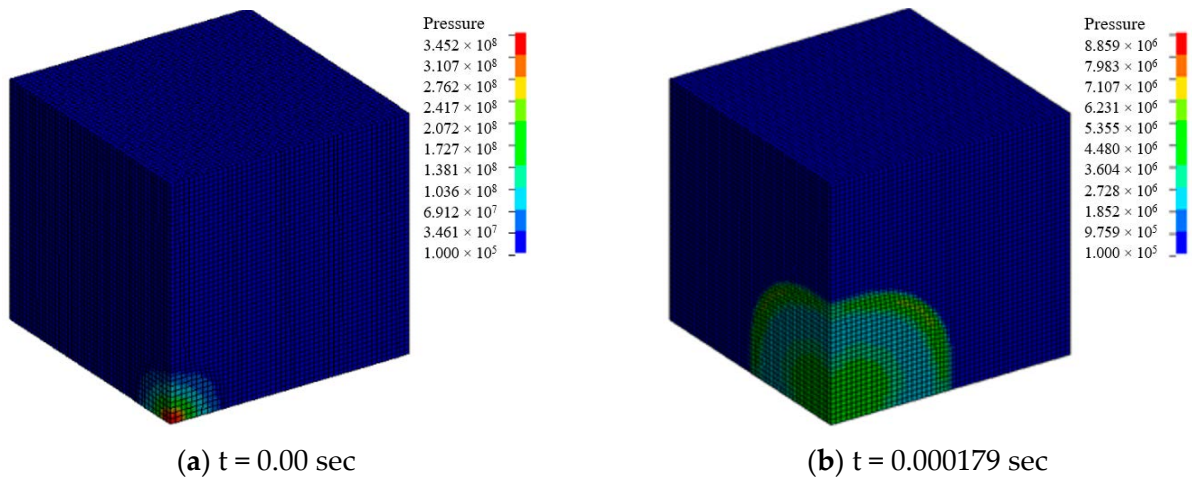


Figure 15. Air blast wave pressure propagation [charge weight = 8 kg].

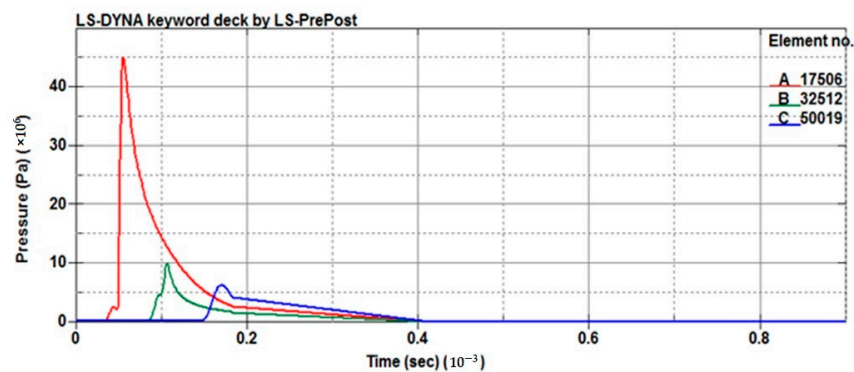


Figure 16. Pressure–time history at different distances (charge weight = 8 kg) using LS-DYNA.

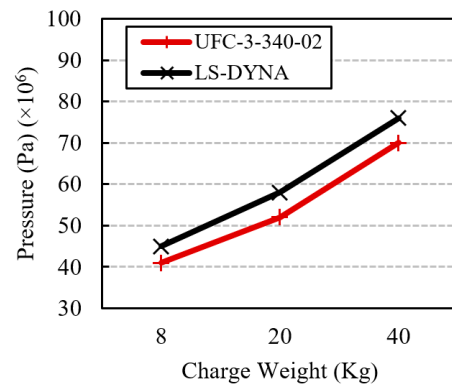


Figure 17. Comparison of pressure results between the LS-DYNA model and UFC-3-340-02 equations.

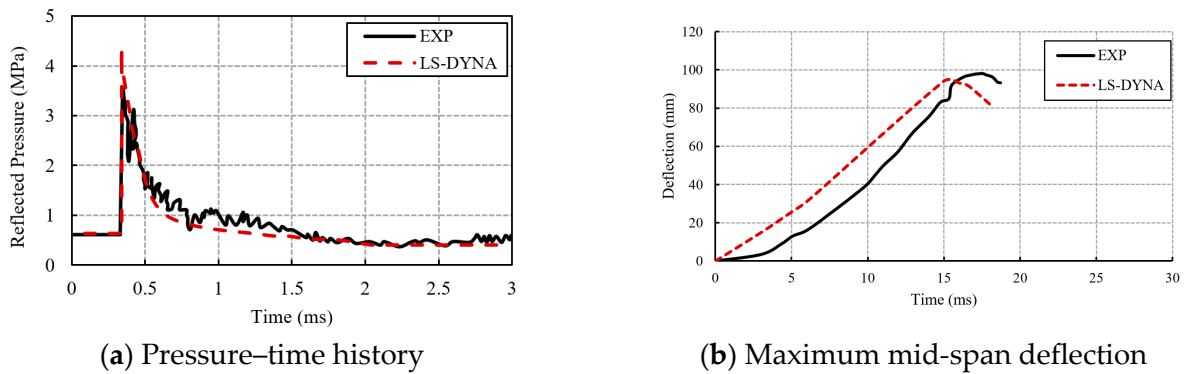


Figure 18. Comparisons of the LS-DYNA and experimental results.

4.2. Comparison between the Different Blast Load Modeling Approaches

The three different approaches (LBE, ALE, and the coupling method, that were discussed earlier) of modeling blast load were compared. The three models produced remarkably similar findings. The ALE model took almost twice as long to complete as the Coupling approach and 15 times as long as the LBE. The Coupling method model took five times as long as the LBE approach to complete. As illustrated in Figure 19, the LBE approach exhibited a lower peak pressure and impulse than the ALE and coupled methods with a difference of less than 15%. The coupled method achieved extremely similar results to the ALE method while consuming significantly less solving time. Therefore, the LBE method was selected for blast modeling due to its computational efficiency and acceptable accuracy. Nevertheless, it is important to note that this selection is applicable to the specific criteria represented within our problem, which involves a simple reinforced concrete beam exposed to a direct blast wave. However, in more complex scenarios, such as simulating the entire structure or when dealing with structural openings, it is recommended to investigate and evaluate the suitability of different approaches. In [59], Schwer et al. provided recommendations for the selection of an air-blast loading technique for close-in charges to improve modeling confidence.

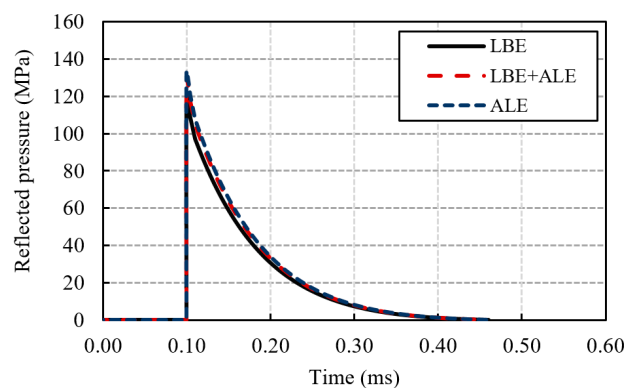
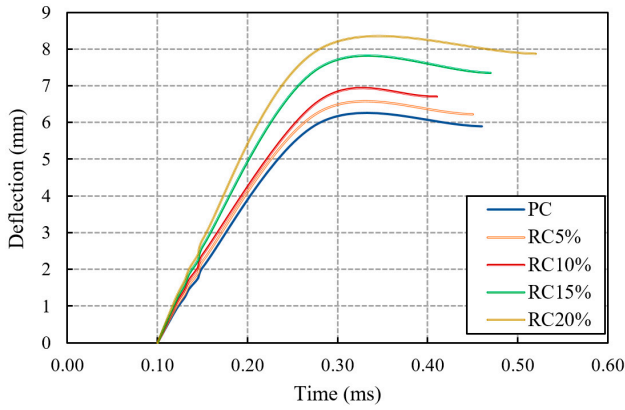


Figure 19. Comparisons of the different blast load modeling approaches.

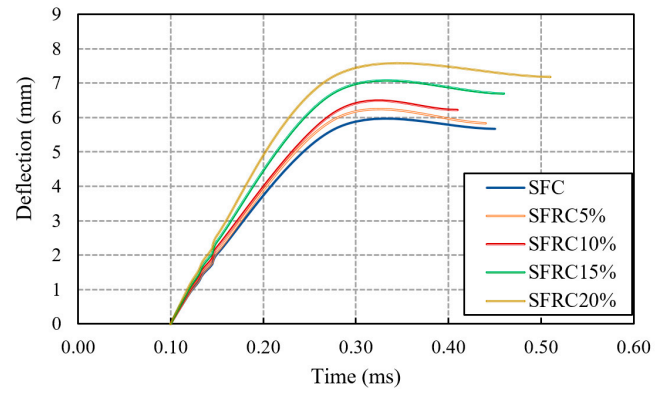
4.3. Rubberized and Rubberized Steel Fiber Concrete Material Response

The validated FE model was used to investigate the responses of the rubberized and rubberized steel fibers RC beams in [28] under blast loads. As shown in Figure 20, the lateral deflections under blast loading are illustrated. A significant increase in deflection was obtained due to the effect of rubber ranging from 5% to 33% when the rubber percentage increased from 5% to 20%, respectively. However, these increases dropped from 3% to 27% when adding steel fibers besides rubber. These findings indicated that as the percentage of rubber increased, ductility improved significantly. The pressure-time history curves of the analyzed models are shown in Figure 21. In addition, Table 6 and Figure 22 provide

the peak reflected pressure and the impulse values for the analyzed models, respectively. The results show that increasing the rubber percentage from 0% to 20% reduced the peak reflected pressure by around 27%, indicating a reduced blast loading capacity. However, the incorporation of steel fibers maintained high ductility and enhanced the blast load capacity, leading to a blast load capacity similar to that of normal concrete with 10% rubber.

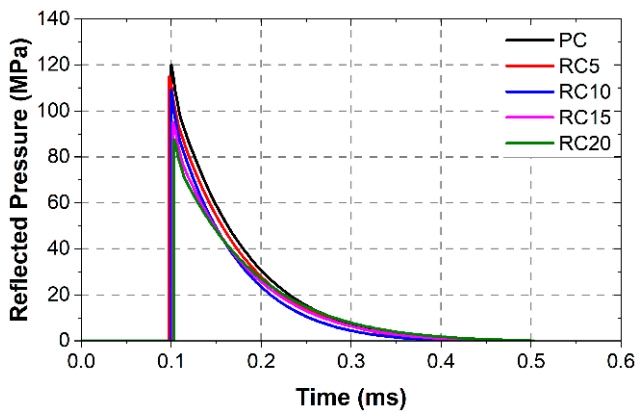


(a) Rubberized concrete models

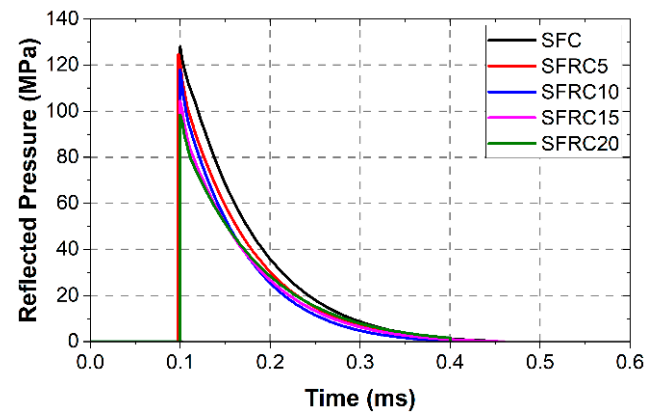


(b) Rubberized steel fiber concrete models

Figure 20. Deflection vs. time curves under blast loads.



(a) Rubberized concrete models



(b) Rubberized steel fiber concrete models

Figure 21. Pressure vs. time history under blast loads.

Table 6. Reflected pressure and impulse.

No	Model Label	Reflected Pressure (MPa)	Impulse (MPa·ms)	No	Model Label	Reflected Pressure (MPa)	Impulse (MPa·ms)
1	PC	120.00	8.22	6	SFC	128.04	9.55
2	RC5%	115.05	7.52	7	SFRC5%	124.80	8.15
3	RC10%	109.09	6.60	8	SFRC10%	118.11	7.14
4	RC15%	95.24	6.90	9	SFRC15%	104.35	6.70
5	RC20%	87.59	7.20	10	SFRC20%	98.36	7.00

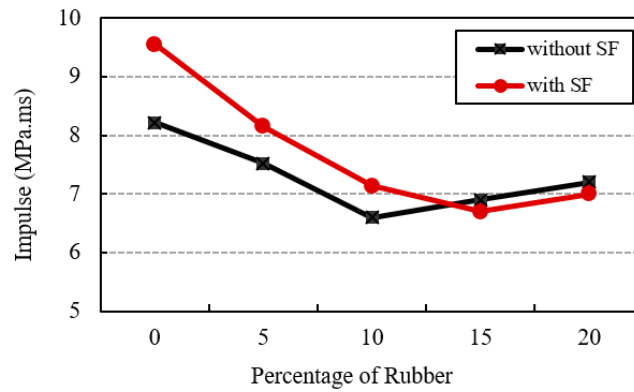
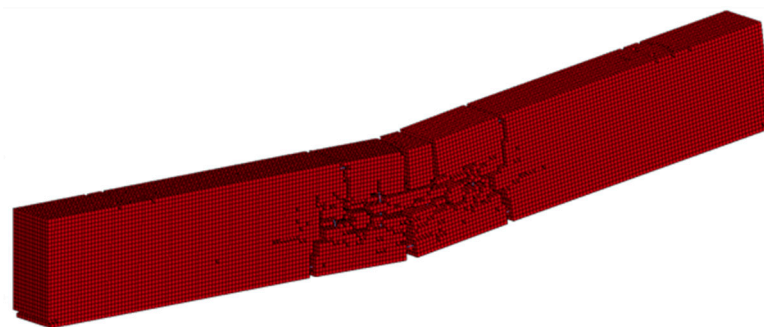
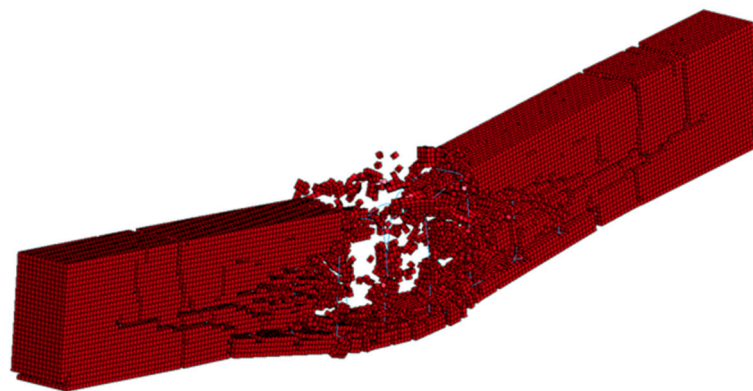


Figure 22. Variation of impulse of rubberized concrete beams with and without steel fibers.

When the rubber percentage increased up to 10%, obvious central bending failure occurred after the explosion and there was no crushing area on the upper side of the beam and no spallation on the bottom side of the beam, as shown in Figure 23a. Similarly, the use of steel fibers with rubber percentages up to 15% resulted in flexural failure without crushing or spalling. On the other hand, when the percentage of rubber exceeds 10%, crushing on the upper side of the beam occurs, in addition to spalling on the bottom of the beam (Figure 23b). The findings confirmed that rubberized concrete exhibited improved energy absorption and ductility when subjected to blast loading compared to conventional concrete. This characteristic could make rubberized concrete a valuable material for applications involving energy dissipation, such as in the construction of sacrificial walls.



(a) Flexural deformation failure



(b) Crushing and spalling failure

Figure 23. Failure modes of the FE models under blast loading.

5. Conclusions

The primary focus of this research revolves around the integration of recycled rubber and steel fibers into concrete, with the ultimate goal of enhancing the dynamic response of RC beams. A meticulous numerical investigation was undertaken to comprehensively assess the static and blast response of these augmented beams. The numerical models were designed to accommodate varying weight percentages of rubber, ranging from 5% to 20%, and a consistent 1.0% incorporation of steel fibers. Utilizing ABAQUS and LS-DYNA, two FE models were meticulously developed and subsequently validated against available experimental data.

1. Static response of concrete is important to ensure the applicability of the concrete for structural engineering design practice and safety margins. The changes in maximum deflection caused by different reinforcement ratios demonstrate the importance of reinforcement design in improving structural integrity. Engineers can improve the stiffness, load-bearing capacity, and overall structural resilience by applying appropriate reinforcement.
2. While rubberized concrete with high rubber content, greater than 10%, showed brittle failure at the compression side, reducing the reinforcement ratio to meet minimum code requirements revealed a notable shift in failure behavior. Specifically, under static loading, the rubberized RC beams tended to exhibit ductile behavior on the tension side.
3. The LBE method showed a lower peak pressure and impulse compared to both ALE and the coupled methods, with differences of less than 15%. Notably, the computational time for the LBE approach was approximately 1/5 to 1/15 times less than that of the other methods. However, in more complex scenarios, such as simulating entire structure or when dealing with structural openings, it is recommended to investigate and evaluate the suitability of different approaches.
4. Increasing the rubber percentage improves ductility and energy absorption, but reduces blast load capacity. However, the incorporation of steel fibers maintains high ductility and enhances blast load capacity, leading to a blast load capacity similar to that of normal concrete with 10% rubber.
5. An optimal concrete mixture characterized by improved ductility, energy absorption, and blast load capacity, achieved by combining 5–10% rubber with steel fibers.

The study has the following limitations. First, the study investigated the blast response of 1D elements, specifically RC beams. However, future studies should explore the blast response of 2D elements, such as RC slabs. Additionally, the blast scenario included in this study targeted the top of the beam with a direct blast wave. However, future investigations should consider exploring different blast locations and structural geometries to broaden the scope of the study.

Author Contributions: Conceptualization, M.T.N., A.S.E. and Y.E.I.; Data curation, M.T.E.; Formal analysis, M.T.E. and A.E.-Z.; Investigation, A.S.E. and M.T.E.; Methodology, M.T.N., A.S.E., M.T.E. and Y.E.I.; Resources, M.T.N., Y.E.I. and A.E.-Z.; Software, M.T.E. and A.E.-Z.; Supervision, M.T.N. and A.S.E.; Writing—original draft, M.T.E.; Writing—review and editing, Y.E.I. and A.E.-Z. All authors have read and agreed to the published version of the manuscript.

Funding: This research received no external funding.

Data Availability Statement: The data presented in this study are available on request from the corresponding author.

Acknowledgments: The authors would like to acknowledge the support of Prince Sultan University for paying the Article Processing Charges (APC) of this publication.

Conflicts of Interest: The authors declare no conflicts of interest.

References

1. Yan, B.; Liu, F.; Song, D.; Jiang, Z. Numerical study on damage mechanism of RC beams under close-in blast loading. *Eng. Fail. Anal.* **2015**, *51*, 9–19. [[CrossRef](#)]
2. Ellingwood, B.R. Mitigating risk from abnormal loads and progressive collapse. *J. Perform. Constr. Facil.* **2006**, *20*, 315–323. [[CrossRef](#)]
3. Goel, M.D.; Matsagar, V.A. Blast-resistant design of structures. *Pract. Period. Struct. Des. Constr.* **2014**, *19*, 04014007. [[CrossRef](#)]
4. Rajkumar, D.; Senthil, R.; Kumar, B.B.M.; AkshayaGomathi, K.; Velan, S.M. Numerical study on parametric analysis of reinforced concrete column under blast loading. *J. Perform. Constr. Facil.* **2020**, *34*, 04019102. [[CrossRef](#)]
5. Cui, J.; Shi, Y.; Li, Z.-X.; Chen, L. Failure analysis and damage assessment of RC columns under close-in explosions. *J. Perform. Constr. Facil.* **2015**, *29*, B4015003. [[CrossRef](#)]
6. Turgut, P.; Gurel, M.A.; Pekgokgoz, R.K. LPG explosion damage of a reinforced concrete building: A case study in Sanliurfa, Turkey. *Eng. Fail. Anal.* **2013**, *32*, 220–235. [[CrossRef](#)]
7. Elbelbisi, A.; Elsis, A.; Saffarini, M.H.; Salim, H.; Chen, Z. Enhanced Blast Response Simulation of LG Panels Using an Elasto-Damage Model with the Finite Element Method. *Buildings* **2023**, *13*, 3025. [[CrossRef](#)]
8. Li, S.; Rong, X.; Hu, J.; Wang, M.; Qu, Q.; Huang, J.; Guo, X. Risk assessment method of gas explosion based on quantification of margins and uncertainties (QMU): A case study on beam structures in buildings. *Structures* **2023**, *50*, 52–62. [[CrossRef](#)]
9. Tai, Y.; Chu, T.; Hu, H.; Wu, J. Dynamic response of a reinforced concrete slab subjected to air blast load. *Theor. Appl. Fract. Mech.* **2011**, *56*, 140–147. [[CrossRef](#)]
10. Leppänen, J. Concrete subjected to projectile and fragment impacts: Modelling of crack softening and strain rate dependency in tension. *Int. J. Impact Eng.* **2006**, *32*, 1828–1841. [[CrossRef](#)]
11. Rabczuk, T.; Eibl, J. Modelling dynamic failure of concrete with meshfree methods. *Int. J. Impact Eng.* **2006**, *32*, 1878–1897. [[CrossRef](#)]
12. Lu, Y. Modelling of concrete structures subjected to shock and blast loading: An overview and some recent studies. *Struct. Eng. Mech. Int. J.* **2009**, *32*, 235–249. [[CrossRef](#)]
13. Elbelbisi, A.; El-Sisi, A.; Mahmoud, M.E.; Newberry, M.; Salim, H. Influence of interlayer types and thicknesses on the blast performance of laminated glass panels. *Structures* **2023**, *57*, 105231. [[CrossRef](#)]
14. Elbelbisi, A.; El-Sisi, A.; Knight, J.; Philipps, J.C.; Newberry, M.; Salim, H. Influence of panels size on the static and dynamic performance of laminated glass panels. *Constr. Build. Mater.* **2023**, *399*, 132562. [[CrossRef](#)]
15. Gong, S.; Lu, Y.; Tu, Z.; Jin, W. Validation study on numerical simulation of RC response to close-in blast with a fully coupled model. *Struct. Eng. Mech. Int. J.* **2009**, *32*, 283–300. [[CrossRef](#)]
16. Brandt, A.M. Fibre reinforced cement-based (FRC) composites after over 40 years of development in building and civil engineering. *Compos. Struct.* **2008**, *86*, 3–9. [[CrossRef](#)]
17. Barnett, S.J.; Lataste, J.-F.; Parry, T.; Millard, S.G.; Soutsos, M.N. Assessment of fibre orientation in ultra high performance fibre reinforced concrete and its effect on flexural strength. *Mater. Struct.* **2010**, *43*, 1009–1023. [[CrossRef](#)]
18. Fehling, E.; Bunje, K.; Schmidt, M. Gärtnerplatz–Bridge over River Fulda in Kassel: Multispan Hybrid UHPC-Steel Bridge. In *Designing and Building with UHPFRC*; John Wiley & Sons, Inc.: Hoboken, NJ, USA, 2011. [[CrossRef](#)]
19. Chin, W.J.; Kim, Y.J.; Cho, J.-R.; Park, J.S. Dynamic characteristics evaluation of innovative UHPC pedestrian cable stayed bridge. *Engineering* **2012**, *4*, 869–876. [[CrossRef](#)]
20. Rebentrost, M.; Wight, G. Perspective on UHPCs from a specialist construction company. In *Designing and Building with UHPFRC*; John Wiley & Sons, Inc.: Hoboken, NJ, USA, 2011; pp. 189–208. [[CrossRef](#)]
21. Ngo, T.; Mendis, P.; Krauthammer, T. Behavior of ultrahigh-strength prestressed concrete panels subjected to blast loading. *J. Struct. Eng.* **2007**, *133*, 1582–1590. [[CrossRef](#)]
22. Barnett, S.J. Development of advanced concrete materials for anti-terrorism applications. *Struct. Eng.* **2008**, *86*, 28–29.
23. Li, J.; Wu, C.; Hao, H. An experimental and numerical study of reinforced ultra-high performance concrete slabs under blast loads. *Mater. Des.* **2015**, *82*, 64–76. [[CrossRef](#)]
24. Vedernikov, A.; Gemi, L.; Madenci, E.; Özkılıç, Y.O.; Yazman, Ş.; Gusev, S.; Sulimov, A.; Bondareva, J.; Evlashin, S.; Konev, S.; et al. Effects of high pulling speeds on mechanical properties and morphology of pultruded GFRP composite flat laminates. *Compos. Struct.* **2022**, *301*, 116216. [[CrossRef](#)]
25. Vedernikov, A.; Tucci, F.; Carlone, P.; Gusev, S.; Konev, S.; Firsov, D.; Akhatov, I.; Safonov, A. Effects of pulling speed on structural performance of L-shaped pultruded profiles. *Compos. Struct.* **2021**, *255*, 112967. [[CrossRef](#)]
26. Elshazli, M.T.; Saras, N.; Ibrahim, A. Structural response of high strength concrete beams using fiber reinforced polymers under reversed cyclic loading. *Sustain. Struct.* **2022**, *2*, 000018. [[CrossRef](#)]
27. Elshazli, M.T.; Ramirez, K.; Ibrahim, A.; Badran, M. Mechanical, durability and corrosion properties of basalt fiber concrete. *Fibers* **2022**, *10*, 10. [[CrossRef](#)]
28. Eisa, A.S.; Elshazli, M.T.; Nawar, M.T. Experimental investigation on the effect of using crumb rubber and steel fibers on the structural behavior of reinforced concrete beams. *Constr. Build. Mater.* **2020**, *252*, 119078. [[CrossRef](#)]
29. Alam, I.; Mahmood, U.A.; Khattak, N. Use of rubber as aggregate in concrete: A review. *Int. J. Adv. Struct. Geotech. Eng.* **2015**, *4*, 92–96.
30. Gupta, T.; Sharma, R.K.; Chaudhary, S. Impact resistance of concrete containing waste rubber fiber and silica fume. *Int. J. Impact Eng.* **2015**, *83*, 76–87. [[CrossRef](#)]
31. Bu, C.; Zhu, D.; Liu, L.; Lu, X.; Sun, Y.; Yu, L.; OuYang, Y.; Cao, X.; Wang, F. Research progress on rubber concrete properties: A review. *J. Rubber Res.* **2022**, *25*, 105–125. [[CrossRef](#)]

32. Prasad, M.G.; Golla, S.Y.; Prabhanjan, N.; Krishna, A.S.; Alok, G. Mechanical properties of rubberized concrete using truck scrap rubber. *Mater. Today Proc.* **2021**, *39*, 849–854. [[CrossRef](#)]
33. He, L.; Cai, H.; Huang, Y.; Ma, Y.; Van Den Bergh, W.; Gaspar, L.; Valentin, J.; Vasiliev, Y.E.; Kowalski, K.J.; Zhang, J. Research on the properties of rubber concrete containing surface-modified rubber powders. *J. Build. Eng.* **2021**, *35*, 101991. [[CrossRef](#)]
34. Huang, W.; Huang, X.; Xing, Q.; Zhou, Z. Strength reduction factor of crumb rubber as fine aggregate replacement in concrete. *J. Build. Eng.* **2020**, *32*, 101346. [[CrossRef](#)]
35. Yu, Z.; Tang, R.; Li, F.; Hu, Y.; Liu, G.; Qin, Y.; Huang, Q. Experimental study and failure criterion analysis on combined compression-shear performance of rubber concrete (RC) with different rubber replacement ratio. *Constr. Build. Mater.* **2021**, *288*, 123105. [[CrossRef](#)]
36. Elshazli, M.T.; Ibrahim, A.; Eidelpes, E.; Ilevbare, G.O. Degradation mechanisms in overpack concrete of spent nuclear fuel dry storage systems: A review. *Nucl. Eng. Des.* **2023**, *414*, 112632. [[CrossRef](#)]
37. Ganjian, E.; Khorami, M.; Maghsoudi, A.A. Scrap-tyre-rubber replacement for aggregate and filler in concrete. *Constr. Build. Mater.* **2009**, *23*, 1828–1836. [[CrossRef](#)]
38. Najim, K.; Hall, M. A review of the fresh/hardened properties and applications for plain-(PRC) and self-compacting rubberised concrete (SCRC). *Constr. Build. Mater.* **2010**, *24*, 2043–2051. [[CrossRef](#)]
39. Onuaguluchi, O.; Panesar, D.K. Hardened properties of concrete mixtures containing pre-coated crumb rubber and silica fume. *J. Clean. Prod.* **2014**, *82*, 125–131. [[CrossRef](#)]
40. Phale, A.R. *Environmental Impact and Waste Management of Used Tyres in the RSA*; University of Johannesburg: Johannesburg, South Africa, 2012.
41. Rashad, A.M. A comprehensive overview about recycling rubber as fine aggregate replacement in traditional cementitious materials. *Int. J. Sustain. Built Environ.* **2016**, *5*, 46–82. [[CrossRef](#)]
42. Shu, X.; Huang, B. Recycling of waste tire rubber in asphalt and portland cement concrete: An overview. *Constr. Build. Mater.* **2014**, *67*, 217–224. [[CrossRef](#)]
43. Kordoghli, S.; Paraschiv, M.; Kuncser, R.; Tazerout, M.; Prisecaru, M.; Zagrouba, F.; Georgescu, I. Managing the environmental hazards of waste tires. *J. Eng. Stud. Res.* **2014**, *20*, 1–11. [[CrossRef](#)]
44. Wang, T.; Xiao, F.; Zhu, X.; Huang, B.; Wang, J.; Amirkhanian, S. Energy consumption and environmental impact of rubberized asphalt pavement. *J. Clean. Prod.* **2018**, *180*, 139–158. [[CrossRef](#)]
45. Jawjit, W.; Kroeze, C.; Rattanapan, S. Greenhouse gas emissions from rubber industry in Thailand. *J. Clean. Prod.* **2010**, *18*, 403–411. [[CrossRef](#)]
46. Yang, X.; You, Z.; Perram, D.; Hand, D.; Ahmed, Z.; Wei, W.; Luo, S. Emission analysis of recycled tire rubber modified asphalt in hot and warm mix conditions. *J. Hazard. Mater.* **2019**, *365*, 942–951. [[CrossRef](#)]
47. Wiśniewska, P.; Haponiuk, J.T.; Colom, X.; Saeb, M.R. Green Approaches in Rubber Recycling Technologies: Present Status and Future Perspective. *ACS Sustain. Chem. Eng.* **2023**, *11*, 8706–8726. [[CrossRef](#)]
48. Li, W.; Wang, Q.; Jin, J.; Li, S. A life cycle assessment case study of ground rubber production from scrap tires. *Int. J. Life Cycle Assess.* **2014**, *19*, 1833–1842. [[CrossRef](#)]
49. Topçu, İ.B.; Demir, A. Durability of rubberized mortar and concrete. *J. Mater. Civ. Eng.* **2007**, *19*, 173–178. [[CrossRef](#)]
50. Grinys, A.; Augonis, A.; Daukšys, M.; Pupeikis, D. Mechanical properties and durability of rubberized and SBR latex modified rubberized concrete. *Constr. Build. Mater.* **2020**, *248*, 118584. [[CrossRef](#)]
51. Thiagarajan, G.; Vasudevan, A.K.; Robert, S. Numerical modeling of concrete slabs reinforced with high strength low alloy vanadium steel bars subjected to blast loads. *Spec. Publ.* **2011**, *281*, 1–16.
52. Schleyer, G.K.; Barnett, S.J.; Millard, S.G.; Wight, G.; Rebertost, M. *UHPFRC Panel Testing*; The Institution of Structural Engineers: London, UK, 2011.
53. Wang, Z.; Wu, J.; Wang, J.-G. Experimental and numerical analysis on effect of fibre aspect ratio on mechanical properties of SRFC. *Constr. Build. Mater.* **2010**, *24*, 559–565. [[CrossRef](#)]
54. Teng, T.-L.; Chu, Y.-A.; Chang, F.-A.; Shen, B.-C.; Cheng, D.-S. Development and validation of numerical model of steel fiber reinforced concrete for high-velocity impact. *Comput. Mater. Sci.* **2008**, *42*, 90–99. [[CrossRef](#)]
55. Mao, L.; Barnett, S.; Begg, D.; Schleyer, G.; Wight, G. Numerical simulation of ultra high performance fibre reinforced concrete panel subjected to blast loading. *Int. J. Impact Eng.* **2014**, *64*, 91–100. [[CrossRef](#)]
56. Liu, Y.; Yan, J.-B.; Huang, F.-L. Behavior of reinforced concrete beams and columns subjected to blast loading. *Def. Technol.* **2018**, *14*, 550–559. [[CrossRef](#)]
57. Ottosen, N.S. A failure criterion for concrete. *J. Eng. Mech. Div.* **1977**, *103*, 527–535. [[CrossRef](#)]
58. Marais, S.; Tait, R.; Cloete, T.; Nurick, G. Material testing at high strain rate using the split Hopkinson pressure bar. *Lat. Am. J. Solids Struct.* **2004**, *1*, 219–339.
59. Schwer, L.; Teng, H.; Souli, M. LS-DYNA Air Blast Techniques: Comparisons with Experiments for Close-in Charges. In Proceedings of the 10th European LS-DYNA Conference 2015, Würzburg, Germany, 15–17 June 2015.

Disclaimer/Publisher’s Note: The statements, opinions and data contained in all publications are solely those of the individual author(s) and contributor(s) and not of MDPI and/or the editor(s). MDPI and/or the editor(s) disclaim responsibility for any injury to people or property resulting from any ideas, methods, instructions or products referred to in the content.